ACS OMEGA

http://pubs.acs.org/journal/acsodf

Article

New Insights into the Metallization of Graphene-Supported Composite Materials—from 3D Cu-Grown Structures to Free-Standing Electrodeposited Porous Ni Foils

Lidija D. Rafailović,* Aleksandar Z. Jovanović, Sanjin J. Gutić, Jürgen Wehr, Christian Rentenberger, Tomislav Lj. Trišović, and Igor A. Pašti

Cite This: *ACS Omega* 2022, 7, 4352−4362

Read Online

ACCESS | Metrics & More | Article Recommendations | Supporting Information

ABSTRACT: The conductivity and the state of the surface of supports are of vital importance for metallization via electrodeposition. In this study, we show that the metallization of a carbon fiber-reinforced polymer (CFRP) can be carried out directly if the intermediate graphene oxide (GO) layer is chemically reduced on the CFRP surface. Notably, this approach utilizing only the chemically reduced GO as a conductive support allows us to obtain insights into the interaction of rGO and the electrodeposited metal. Our study reveals that under the same contact current experimental conditions, the electrodeposition of Cu and Ni on rGO follows significantly different deposition modes, resulting in the formation of three-dimensional (3D) and free-standing metallic foils, respectively. Considering that Ni adsorption energy is larger than Ni cohesive energy, it is expected that the adhesion of Ni on rGO@CFRP is enhanced compared to Cu. In contrast, the adhesion of deposited Ni is reduced, suggesting diffusion of H^+ between rGO and CFRP, which promotes the hydrogen evolution reaction (HER) and results in the formation of free-standing Ni foils. We ascribe this phenomenon to the unique properties of rGO and the nature of Cu and Ni deposition from electrolytic baths. In the latter, the high adsorption energy of Ni on defective rGO along with HER is the key factor for the formation of the porous layer and free-standing foils.

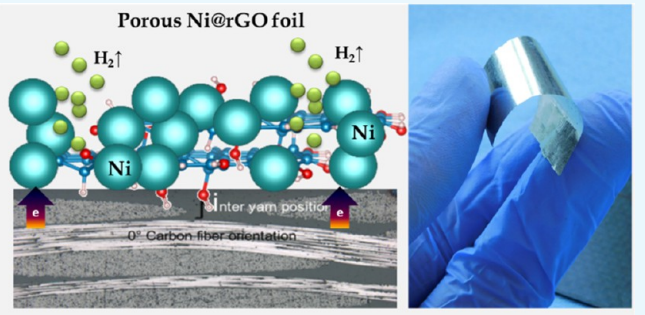

INTRODUCTION

Since its discovery in 2004,[1] graphene, a single sheet of two-dimensional (2D) sp^2-hybridized carbon atoms, attracted researchers' enormous attention over the world. Owing to its unique electronic, optical, and mechanical properties, the use of graphene-based materials in electrochemistry is of special interest, showing promising applications in the fields of supercapacitors, energy storage and conversion, sensing, field-effect transistors, and others.[2−4] Regarding large-scale production, the cost-effective chemical synthesis routes by reducing graphene oxide (GO) seem a suitable choice since GO is easily suspended in aqueous media and could be deposited on various substrates.[5−7] Among various approaches for reducing GO such as using photocatalytic, electrochemical, or thermal procedures, the chemical approach was recognized as a promising method for mass production of graphene sheets that yields graphene-based materials with a significant amount of retained oxygen groups and defects.[7] Initially, oxidized graphite oxide is exfoliated into graphene oxide, allowing separation of layers despite the initial high cohesive energy of the π stacked layers in graphite (5.9 kJ mol^{-1}).[4] Chemical functionalization achieved by oxidation of graphite[8] results in the predominant formation of hydroxyl and epoxy functional groups on the basal carbon plane of GO and is followed by its reduction by different chemical agents, most commonly hydrazine hydrate or, more recently, ascorbic acid.[9] Although the chemically derived graphene cannot fully match single-layer graphene properties, i.e., mechanically exfoliated graphene, the chemical synthesis route to achieve reduced GO (rGO) offers a cost-effective, large-scale production method that can extend its possible field of applications. Furthermore, the formation of graphene-based composites opens even more directions for possible applications, making this material an excellent platform in numerous technologies. As one of the examples, it is possible to mention novel electrocatalysts for the hydrogen evolution reaction (HER) in alkaline media.[10,11] In this case, a subtle interplay between Ni and rGO at the interfacial region enables the dynamics of the

Received: November 2, 2021
Accepted: January 12, 2022
Published: January 27, 2022

https://doi.org/10.1021/acsomega.1c06145
ACS Omega 2022, 7, 4352−4362

HER intermediate and significantly boosts hydrogen production.

Metallized carbon fiber-reinforced polymer (CFRP) substrates are used in many fields, including aerospace applications. The development of advanced CFRP metallic composites, particularly Cu, Ni, and their alloys realized through an electrochemical deposition process has been a subject of intensive work.[12,13] Surface metallization of CFRP yields a conductive surface and brings benefits of both metals and composites, minimizing the amount of metal required for electrostatic discharge and electromagnetic interference—radiofrequency interference shielding and/or protection against lightning strikes and earthing for on-board electronics. Here, we demonstrate a procedure for producing free-standing rGO—metal foils by metallization of nonconductive CFRP substrates modified by rGO. In this approach, the reduction of GO directly on the epoxy-based composite renders the surface sufficiently conductive to perform the direct electroplating step. Hence, it is possible to avoid using many chemicals mandatory to pretreat and activate the polymer or the CFRP surface before the first electroless metallization step that provides a conductive surface of the polymer before the electroplating metallization step. Hence, by fabricating rGO directly on the CFRP surface, direct metal electrodeposition is possible.

Further, we have found that identically prepared rGO supports on CFRP lead to significant differences regarding the electrodeposition process of Cu and Ni and the adhesion and properties of the corresponding deposits. This is of crucial importance, as both Cu and Ni have found broad applications in electronics, metal protection, and catalysis, to mention a few. In addition to the mechanical strength, reinforced carbon-based metallic composites are excellent multifunctional materials in terms of electrical and thermal conduction.[14] We have shown that Cu layers grow preferentially above the carbon fibers of the laminate and show good adhesion with the support. In contrast, Ni ion reduction, accompanied by extensive hydrogen evolution, causes the fabrication of free-standing porous Ni foils.

RESULTS AND DISCUSSION

rGO-Modified CFRP. Raman spectroscopy is a well-established tool for the identification of graphene-based structures.[5] Typically, the Raman spectrum of graphene shows two characteristic peaks: one peak, denoted by G, is located at ∼1580 cm^{-1} and originates from in-plane vibrations of sp^2-bonded carbon atoms, whereas the G′ (2D) peak at 2700 cm^{-1} is generated by a second-order Raman scattering process.[5] The intense peak denoted by D at ∼1350 cm^{-1} is due to out-of-plane vibrations and is attributed to defects and functional groups in the structure. The Raman spectrum of CFRP modified by rGO (Figure 1) shows the D, G, and 2D bands represented by peaks at 1347, 1583, and 2684 cm^{-1}, respectively, using 532 nm laser excitation. However, in a detailed analysis, Raman spectra are often fitted with several additional peaks. Therefore, to obtain detailed information, the rGO@CFRP Raman spectrum was deconvoluted to five peaks between 1000 and 1700 cm^{-1}, and two peaks in the 2500—3000 cm^{-1} region, using Gaussian and pseudo-Voigt functions in Fytik software. The fitted spectrum (cf. Figure 1) shows designated peaks taken for further detailed analysis. The relative content of structural defects was evaluated by the ratio of intensities and areas of D and G peaks after the fitting: the

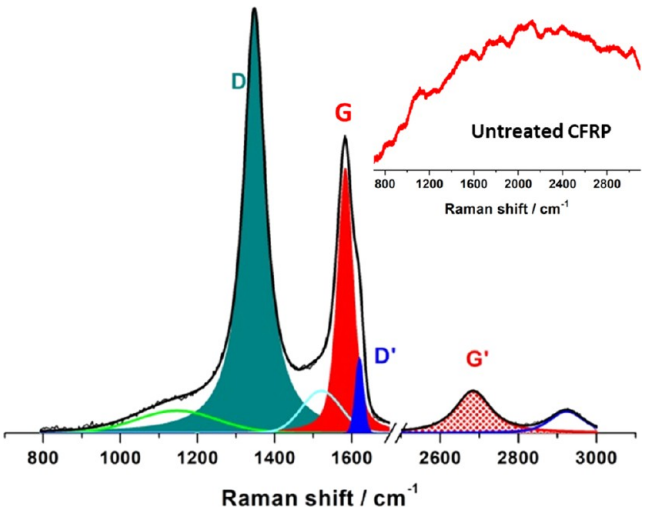

Figure 1. Raman spectra of rGO-modified CFRP. The four peaks used for the analysis are indicated. The inset shows the Raman spectra of untreated CFRP.

I_D/I_G ratio was found to be 1.58, while the A_D/A_G ratio was 2.68. Both numbers indicate a significant number of defects, which is important if graphene-based materials are intended for use in electrochemical systems.

Furthermore, the full width at half-maximum (FWHM) for the G′ (2D) peak (108 cm^{-1}, observed at 2684 cm^{-1}) is significantly higher compared to the FWHM value of 20 cm^{-1} usually observed for single-layer graphene, which could lead to the conclusion that rGO in the rGO@CFRP composite is dominantly multilayered.[15] The high symmetry of the G′ peak (i.e., the absence of several overlapping peaks) points to the possibility of the turbostratic nature of carbon.[15] The origin of the additional peaks, as well as their number, is still under debate.[16] Nevertheless, there are well-documented empirical relationships between the structural features and the emergence of some of these bands.[17] The ratio of the D′ (observed at 1620 cm^{-1}) and D band intensities can be used to evaluate the relative contribution of the sp^3 defects, vacancies, and edges to the total number of defects.[17,18] An $I_D/I_{D'}$ ratio of 5.50 for rGO@CFRP is in accordance with the expected structure of the reduced graphene oxide, with a number of vacancy defects but with low content of sp^3 carbons. Further detailed analysis of the Raman results of rGO and metallized rGO is given in the section Free-Standing Metal@rGO Composite Foils. It should be noted that the untreated CFRP surface has no detectable signal due to the strong fluorescence of the epoxy-based composite polymer (inset of Figure 1).[19]

The composite, which was not modified by rGO, exhibits an average roughness R_a of about 0.2 μm, which is not significantly influenced by the reduction process achieved on GO transferred onto the composite. It can be assumed that, in addition to de-epoxidation of GO by hydrazine, the epoxy-based composite polymer undergoes the epoxy ring opening and formation of hydroxyl groups during reduction and dihydroxylation by the moderate heat treatment, efficiently functionalizing rGO to support.[7,20]

The verification of the reduction of GO directly on the CFRP surface as an approach that could be utilized to yield a surface-functionalized graphene-based composite material is revealed from the conductivity measurements. Above the

https://doi.org/10.1021/acsomega.1c06145
ACS Omega 2022, 7, 4352−4362

carbon fibers in the laminate, localized in situ scanning electron microscopy (SEM) impedance measurements show the typical semicircle in the Nyquist diagram and give a value of the electronic resistance of rGO of ca. 2 kΩ calculated from a composite surface area of 1 cm^2 (cf. Figure S1 in the Supporting Information). Although this area is partially conductive (also reflected in direct electroplating, see further Figure 2a−c due to the vicinity of carbon fibers covered with a 1 μm thick epoxy as confirmed in the SEM cross section image, i.e., top yarn laminate position (cf. Figure S2 in the Supporting Information)), the same area before modification by rGO yielded no measurable current−voltage characteristics due to high ohmic resistance. It is known that GO behaves as an electrical insulator due to the presence of oxygen functionalities, disrupting sp^2 networking.[7,21] Therefore, this result further supports the reduction of rGO on the composite by deoxygenation of GO.

Metallization of rGO-Modified CFRP. The functionalization of the CFRP support enabled one-step direct electroplating on initially poorly conductive CFRP. Namely, in our previous report on metallization of CFRP, we have shown that surface pretreatment is a key step to achieve an adherent metallic layer.[13] Formation of functional, predominantly hydroxyl groups and accompanying roughening of the polymer composite by plasma or chemical activation are essential steps to obtain an adherent metallic layer. Here, we created an intermediate rGO layer bonded to a composite surface that enables surface metallization by the galvanic Cu and Ni layer in the next step.

Figure 2 shows the results of the electrodeposition of Cu and Ni on both untreated and rGO-functionalized CFRP surfaces. Untreated substrates could be plated selectively on particular laminate composite areas only. These regions correspond to the areas where carbon fibers were close to the outer CFRP surface (with a thickness of the above epoxy layer of about 1 μm as deduced from the SEM images made on cross sections (cf. Figure S2 in the Supporting Information)). Figure 2a,b represents these top yarn CFRP areas, showing loosely attached large Cu and Ni particles only above carbon fiber areas in the laminate. In contrast, continuous metallic layers on a large area of approximately 15 cm^2 were deposited on rGO-modified CFRP. This result is a direct consequence of surface functionalization of CFRP by rGO and enhanced conductivity brought by this interim rGO layer (Figure 2c,d). Therefore, the images of Ni- and Cu-plated layers reveal pronounced differences achieved by electrodeposition of identically treated supports, indicating a predominant influence of the surface-functionalized rGO composite substrates and plating conditions on Ni and Cu layer growth.

To obtain insights into the adhesion of Cu and Ni layers electrodeposited on rGO-modified CFRP supports, qualitative adhesion tests are carried out by cross-cut testing. The results of cross-cut and soft scratching tests show that the electrodeposited Ni layer easily peels off from the surface. This result contrasts with the case of Cu, although the Cu layer electrodeposited on the rGO-modified CFRP support is also not adhesive enough to allow direct applications.

SEM images of Cu deposits show island growth of Cu (Figure 3a), thus supporting the previously observed morphology and nucleation kinetics of Cu island formation on the Au working electrode during electrodeposition monitored by in situ transmission electron microscopy (TEM).[22] In the case of Ni, the presence of holes and depressions in the continuous layer is clearly visible, which can unambiguously be ascribed to the accompanying HER during the Ni electrodeposition process (Figure 3b). The occurrence of HER during Ni deposition is not surprising, as Ni is a rather

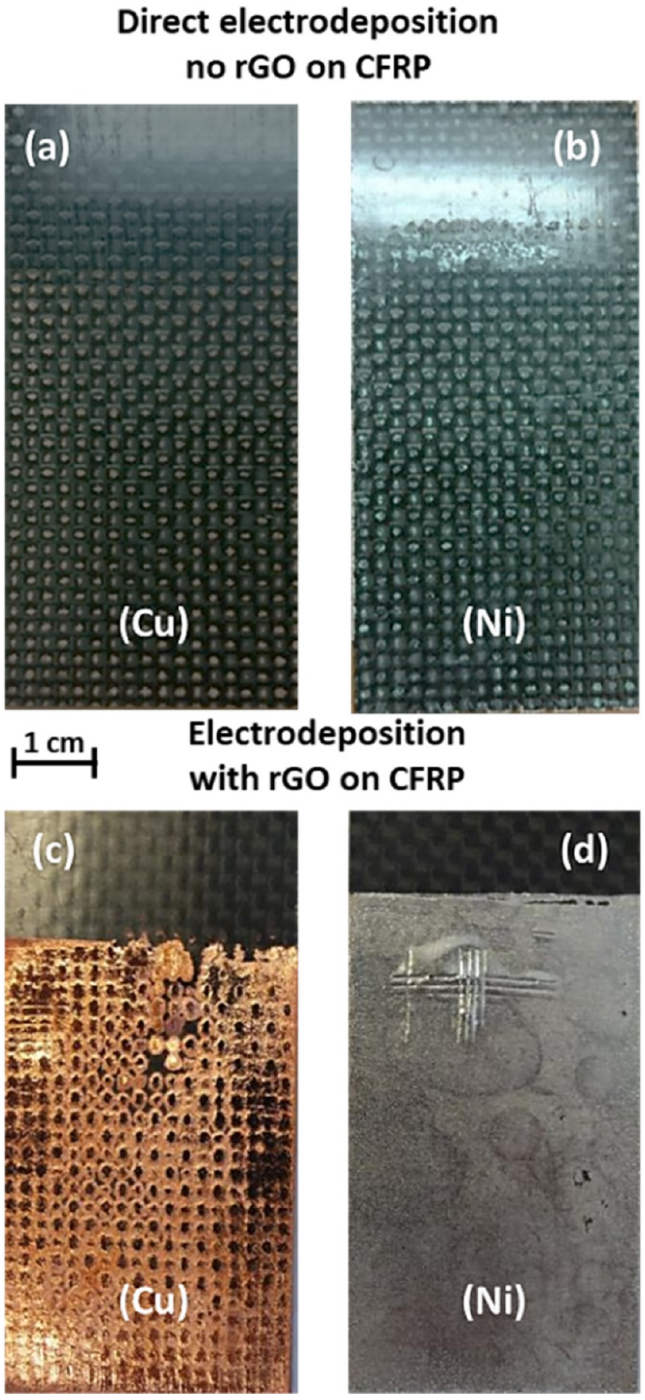

Figure 2. Photographs of Cu and Ni metallized CFRP surfaces (a, b) before and (c, d) after modifications of composite CFRP substrates by the intermediate interface rGO layer: (a) Cu and (b) Ni direct electrodeposition showing only partially plated areas in the vicinity of the carbon fibers in the laminate, (c) rough Cu preferentially grown above the carbon fiber in the laminate, and (d) continuous Ni layer. Layers of (c) Cu and (d) Ni on CFRP composite surfaces are only achieved by electrodeposition in cases of previous modification of composites by reduction of chemically deposited GO directly on the CFRP surface.

https://doi.org/10.1021/acsomega.1c06145
ACS Omega 2022, 7, 4352−4362

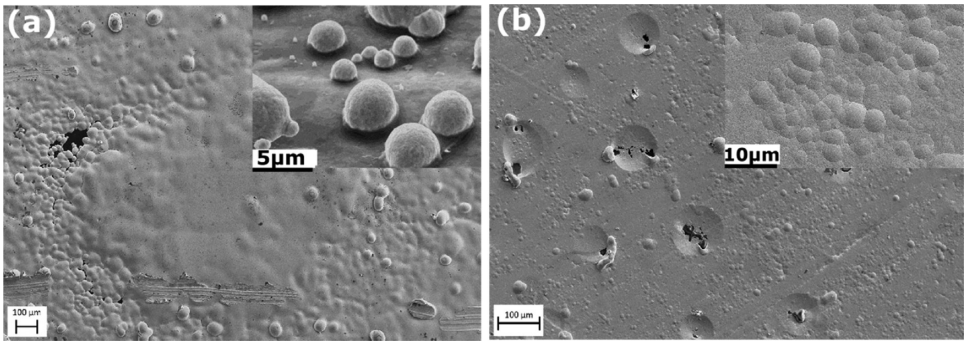

Figure 3. Surface topography SEM images of Cu- and Ni-electroplated rGO-modified CFRP supports: (a) morphology of the Cu surface showing preferential growth above the carbon fibers in the laminate; the inset shows the more detailed growth of Cu 3D particles formed around these areas. (b) Morphology of the Ni surface showing holes and spherical depressions where extensive hydrogen evolution occurred; the inset reveals more detailed insights into the topology of the continuous Ni layer showing the boundaries of coalesced particles.

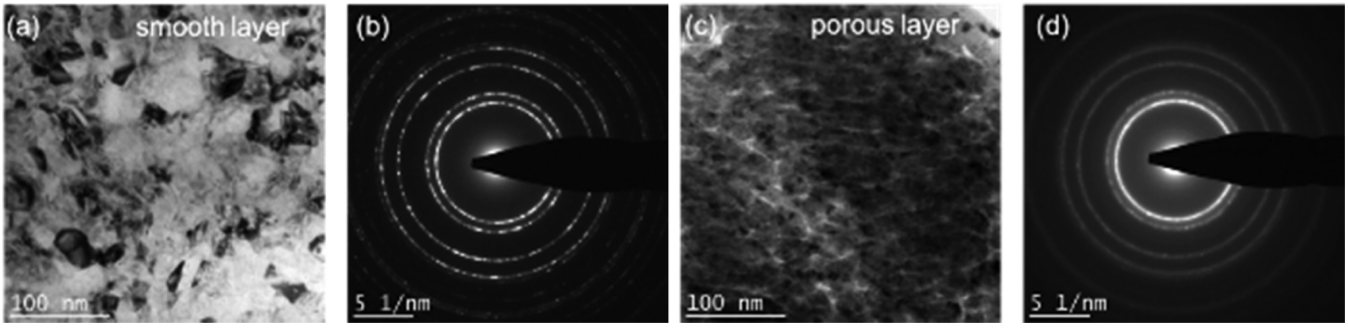

Figure 4. TEM bright-field and diffraction images of the Ni deposit at two different areas referring to a smooth layer (a, b) and a porous layer (c, d).

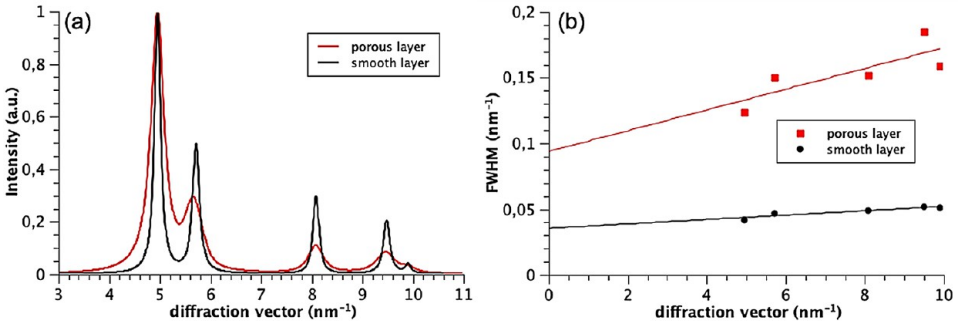

Figure 5. Evaluation of the diffraction patterns taken from the porous and smooth area of the Ni deposit. (a) Intensity profile of the diffraction profile obtained by integration along rings. (b) Plot of the full width at half-maximum (FWHM) as a function of diffraction vector indicates a smaller crystallite size and a larger internal strain of the porous layer.

good HER catalyst and certainly much more active than Cu.[10,23]

To obtain the information on the mechanical properties of all deposited layers, i.e., rGO and Cu@rGO and Ni@rGO composites, we performed nanoindentation measurements. The obtained results suggest that the mechanical properties are governed by the nature and structure of the metallic layer preferentially; the Ni@rGO composite shows 4-fold higher hardness than the Cu@rGO composite (Figure S3 in the Supporting Information). This result is consistent with the Hall−Petch relation, yielding a 3.7 times stronger material with a decrease in the crystallite size calculated from X-ray diffraction (XRD) patterns that show well-defined peaks of a face-centered crystallographic structure (cf. Figure S4 in the Supporting Information). The obtained crystallite size for Ni is 17 nm compared to 250 nm for Cu (Figure S4 in the Supporting Information). The hardness of the rGO@CFRP support is comparable or slightly increased upon the modification with rGO.

Detailed structural characterization of the Ni deposit was carried out by TEM (Figure 4). Two different types of structures within the Ni layer could be identified. Figure 4a,b displays the bright-field image and the corresponding diffraction pattern of the layer area, showing a smooth surface. The contrast variations in the bright-field image indicate crystalline grains of given orientations below 100 nm containing some lattice defects. Both images point to a nanocrystalline face-centered cubic (fcc) structure with no preferred texture, i.e., the crystallographic orientation of the small grains is random. The bright-field image of the porous

https://doi.org/10.1021/acsomega.1c06145
ACS Omega 2022, 7, 4352−4362

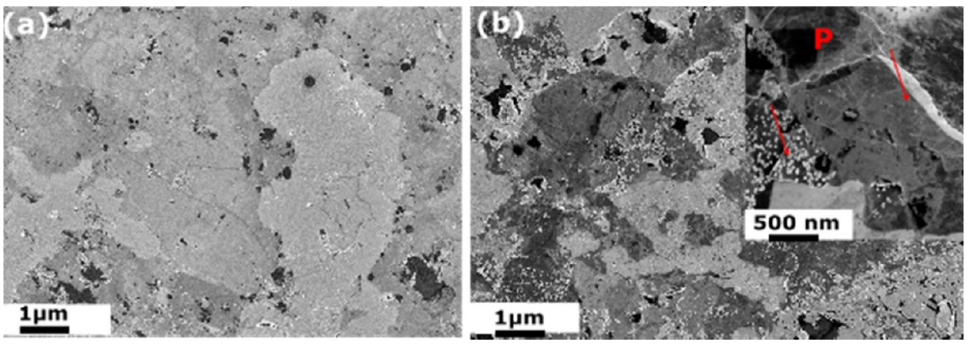

Figure 6. In-lens SEM images of rGO@Cu and rGO@Ni detached from the composite support showing (a) the existence of rGO mostly in monolayers at the interface with Cu, indicating good adhesion of Cu on the CFRP support, and (b) the presence of rGO in multiple layers or wrinkled sheets at the interface with Ni; the inset shows deposited Ni metallic particles below 100 nm in size both between sheets and on the edges of rGO sheets (denoted P in inset).

layer (Figure 4c) shows linear bright contrast features around grains or the assembly of grains. These contrast features indicate local thickness variations and the presence of pores between the grains on a nanometer scale. The diffraction image shows a ring pattern corresponding to the fcc structure of Ni.

To obtain additional information on the two areas, intensity profiles of both diffraction patterns were calculated (Figure 5a). The porous layer area shows an intensity profile with considerably broader peaks than that of the smooth layer area. In Figure 5b, the FWHM values of both sample areas are plotted as a function of the diffraction vector (Williamson–Hall plot). Two main results can be derived from the plot: the absolute FWHM values and the slope are higher for the porous layer area. Since the intercept with the *y*-axis relates inversely to the crystallite size,[24] this size is about 2.5 times smaller in the porous area, whereas the higher slope indicates about 4 times higher mean square strain. Therefore, it is concluded that the porous layer area comprises assembles of crystallites separated by nanosized pores. The crystallites have a size of about 10 nm and contain high internal strains. On the other hand, the smooth layer area shows a nanocrystalline structure with larger crystallites of about 25 nm and considerably lower internal strains. The crystallite size values are in good agreement with an average crystallite size of 17 nm measured by XRD.

Free-Standing Metal@rGO Composite Foils. As deduced from the investigation of the adhesion of metallized layers, Cu, and Ni show pronounced differences in their growth over the rGO-modified CFRP supports. This effect can only be ascribed to the influence of the intermediate interface rGO layer. Therefore, to probe the quality of rGO attached to the metallic layers and some particularities of the metal–rGO interface, Cu@rGO and Ni@rGO were peeled off from the CFRP substrate. Figure 6 shows the SEM images of the remained rGO-modified support on Cu or Ni foils. It reflects indirectly both the adhesion strength between the metal and the support and the role of the interim rGO layer. As shown in Figure 6, almost a continuous rGO over the Cu layer remains, while in the case of Ni, particles deposited between the wrinkled graphene sheets on the edges are present (cf. Figure 6).

To obtain more detailed structural information about the rGO layers that remained at the Cu or Ni interface, Raman spectra of these free-standing foils were collected at several different locations. Selected Raman spectra of these samples, deconvoluted in the same manner as the spectrum for rGO@CFRP (cf. Figure 1) with assigned bands, are shown in Figure 7. Compared to the spectrum of rGO@CFRP, two additional peaks are resolved in the spectral region above 2500 cm^{-1} (cf. Figure 7). Corresponding parameters obtained from all of the collected spectra (including parameters of rGO@CFRP) are listed in Table 1. Positions of D, G, D′, and G′ bands for the metal–rGO interface do not vary significantly at different

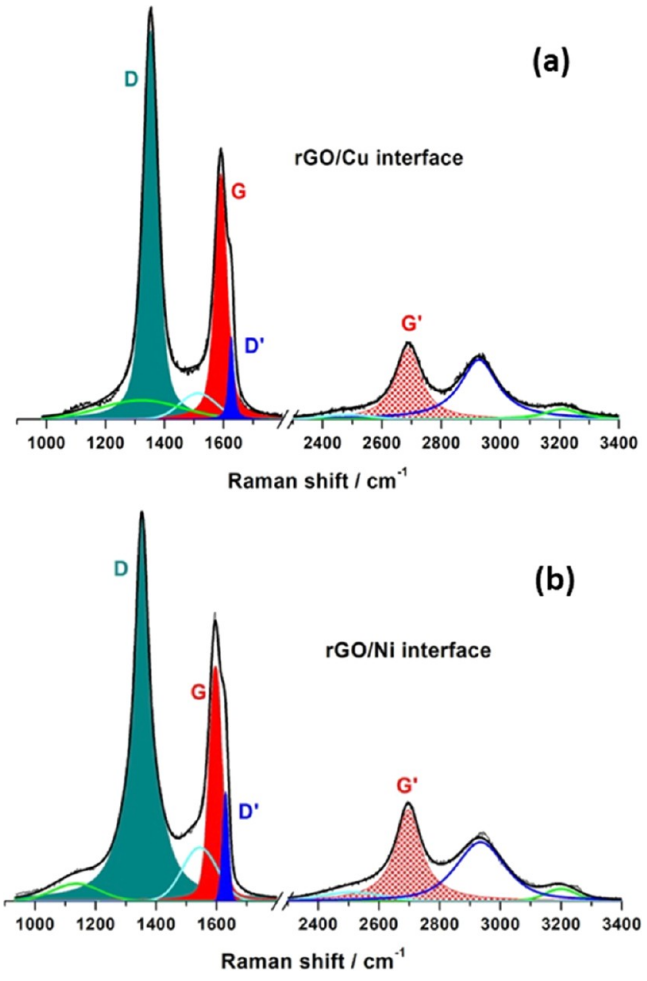

Figure 7. Raman spectra of rGO at the interface with (a) Cu and (b) Ni electrodeposited on the rGO-modified CFRP substrate surface. The indicated peaks are evaluated concerning intensity, area, and position.

https://doi.org/10.1021/acsomega.1c06145
ACS Omega 2022, 7, 4352–4362

Table 1. Intensity, Peak Positions, and Intensity/Area Ratios Calculated from Raman Spectra of rGO@CFRP, Cu@rGO, and Ni@rGO

	Raman shift (cm^{-1})			
	D	G	D′	G′ (2D)
rGO@CFRP	1347	1583	1620	2684
Cu@rGO	1353.2 ± 1.1	1591.8 ± 1.8	1625.6 ± 1.1	2695.2 ± 4.8
Ni@rGO	1352.3 ± 1.2	1594.3 ± 1.5	1626.7 ± 0.6	2693 ± 10
	FWHM (cm^{-1})			
	D	G	D′	G′ (2D)
rGO@CFRP	68	49	26	108
Cu@rGO	64.2 ± 4.8	47.8 ± 0.9	22.8 ± 0.8	103 ± 10
Ni@rGO	61 ± 3	43 ± 7	28.0 ± 1.7	109 ± 13
	peak intensity/area ratios			
	I_D/I_G	A_D/A_G	$I_{G'}/I_G$	$I_D/I_{D'}$
rGO@CFRP	1.58	2.68	0.158	5.50
Cu@rGO	1.42 ± 0.10	1.95 ± 0.05	0.26 ± 0.02	3.7 ± 0.5
Ni@rGO	1.59 ± 0.22	2.68 ± 0.37	0.37 ± 0.01	4.29 ± 0.03

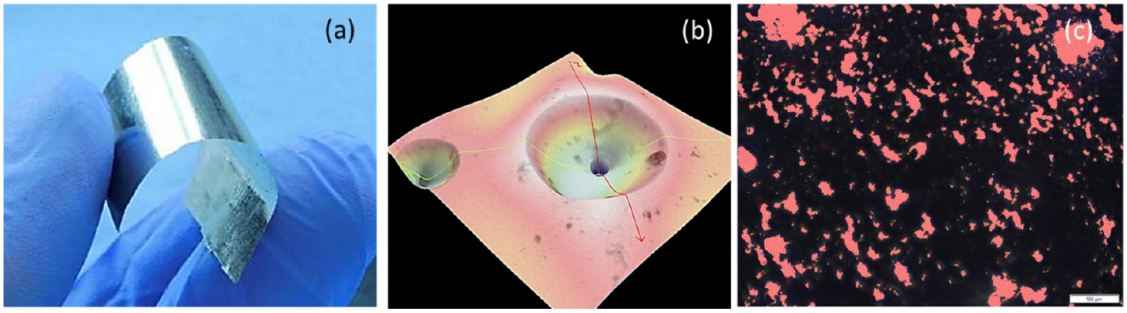

Figure 8. (a) Free-standing porous Ni@rGO foil obtained upon Ni electrodeposition on the rGO-modified composite with a part of the CFRP substrate seen as black in the background, (b) SEM 3D reconstruction of a single pore left upon H_2 templating, going through the entire foil thickness (shown line profiles indicate a foil thickness of 40 ± 10 μm; the reconstructed area is 100 × 100 μm^2), and (c) optical microscopy of the porous free-standing Ni@rGO foil, indicating the high density of pores with different sizes (scale bar: 100 μm).

locations, while ratios of different band intensities show variations, suggesting some degree of inhomogeneity in terms of the rGO structure. By comparing Raman parameters for rGO@CFRP, Cu@rGO, and Ni@rGO, the following important observations need to be underlined: (i) metals cause blue shifts of all four bands (Table 1); (ii) I_D/I_G (as well as A_D/A_G) has the same value(s) for rGO@CFRP and Ni@rGO but decreases for Cu@rGO; (iii) $I_{G'}/I_G$ (as well as $A_{G'}/A_G$) increases in the rGO@CFRP > Cu@rGO > Ni@rGO order; (iv) D and G peaks become narrower, while D′ becomes wider for Ni@rGO but narrower for Cu@rGO samples compared to rGO@CFRP; (v) the FWHM of G′ has comparable values for all of the samples (except for one location on the Cu@GO interface); and (vi) the $I_D/I_{D'}$ ratio for rGO@CFRP is 5.50, while for metal@rGO samples, it is <4.0. The relative shift of the G and G′ band positions for metal@rGO samples (with respect to the positions for rGO@CFRP) can be the consequence of two different effects: graphene doping by the metal, which strongly influences the G band position due to the alteration in sp^2 bonding thorough the charge transfer,[25] and mechanical strain induced by the mismatch between the metal and the graphene lattice, which has a strong influence on the G′ position, due to the phonon-induced intraband electronic transitions.[25] The former effect is hard to elucidate in the case of high mechanical strain.[26] In the cases of Ni@rGO and Cu@rGO, both G and G′ bands are blue-shifted, which indicates p-type doping of graphene.[27] The change of the peak positions relative to the positions for rGO@CFRP is comparable for G and G′ bands: ∼10 cm^{-1}, which could be due to a similar contribution of doping and mechanical strain. However, the lattice mismatch between Ni and graphene is less than 1.2%,[25] excluding mechanical strain at the contact between metal and graphene as a dominant effect. Furthermore, the domination of a particular effect depends also on metallic particle size; peak shifts for smaller particles indicate doping, while those for larger ones are due to mechanical strain.[26] On the other hand, the strong interaction between Ni atoms and vacancies in rGO[28] does not allow the significant formation of a pure metal phase for composites prepared by electrochemical metal deposition, enhancing the possibility of significant mechanical strain in the case of Ni@rGO. Together with a small size of Ni crystallites, this effect is responsible for comparable shifts of G and G′ bands. The same shift observed for Cu@rGO is also a consequence of the combined effects, with the difference being in the size of Cu crystallites, which give rise to significant mechanical strain. Apart from the I_D/I_G (or A_D/A_G) ratio, which is used as a parameter for estimating a relative number of defects, the ratio of the intensities of D and D′ bands can be used to distinguish the contributions from different types of defects.[17] The values of $I_D/I_{D'}$ close to 7 are observed for vacancies, while the values close to 3.5 emerge due to edges in real graphene structures. Our results suggest that interaction of electrodeposited metals with rGO leads to "graphene healing phenomena", also

https://doi.org/10.1021/acsomega.1c06145
ACS Omega 2022, 7, 4352−4362

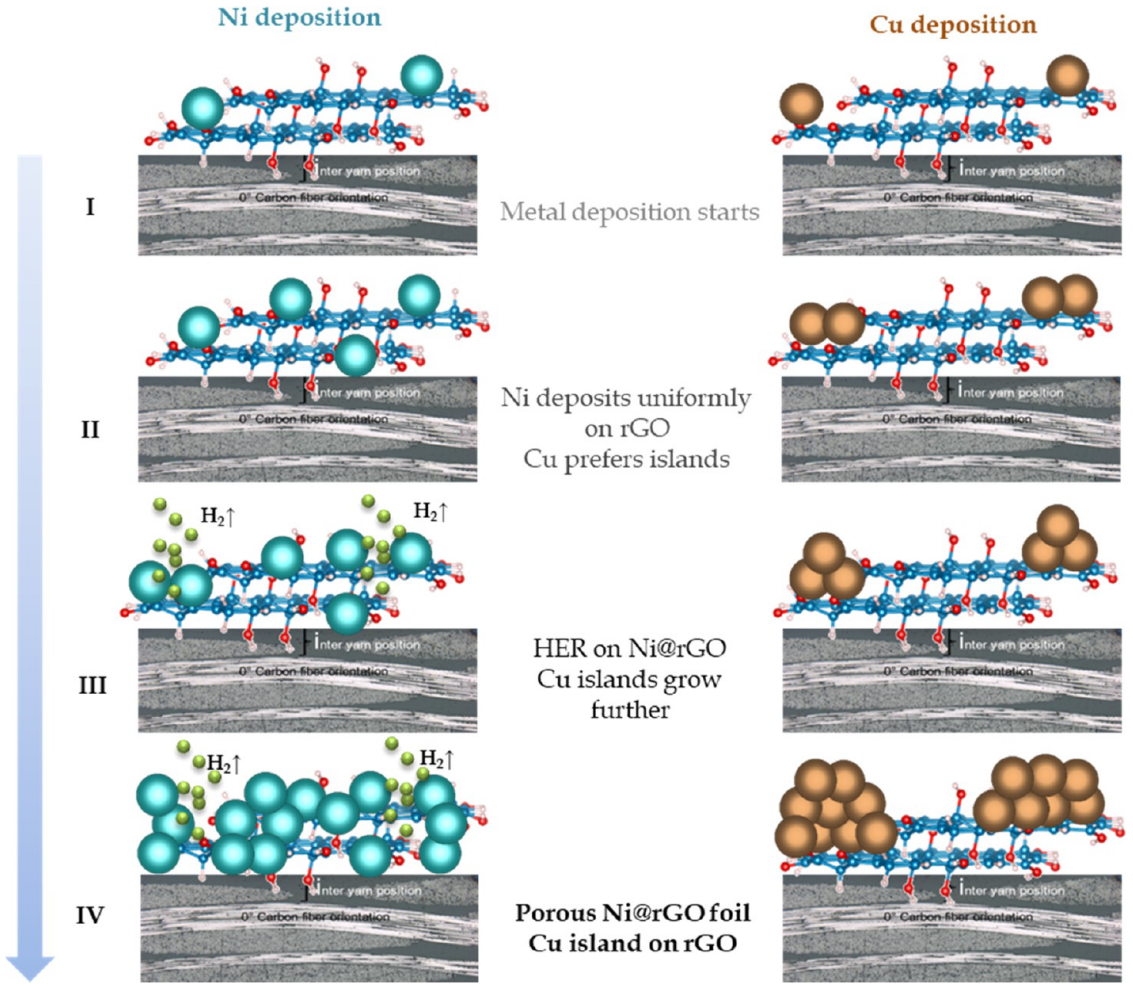

Figure 9. (I) Initial step: the rGO/@CFRP support immersed into the Ni or Cu plating electrolyte. (II) Start of electrodeposition: nucleation of Ni or Cu metallic particles on the rGO@CFRP support. (III) The build-up of a metallic Ni layer on top of the rGO@CFRP support, showing simultaneous attachment of hydrogen bubbles during the growth and suppressing the further supply of electroactive species (in contrast to Cu). As a result, a porous Ni@rGO foil is obtained (IV), while large islands of Cu are grown on rGO.

observed by other authors,[29] i.e., metal atoms "mask" vacancies in terms of Raman spectroscopy. This is evident if the $I_D/I_{D'}$ value for rGO@CFRP (5.50) is compared with values for Cu@rGO (3.66) and Ni@rGO (3.98, Table 1).

Model of Cu and Ni Interactions with rGO Proposing Electrodeposition Conditions that Favor the Formation of Free-Standing Ni@rGO Foils. Evidently, deposition modes and adhesion at the interface between Ni@rGO and Cu@rGO seem to differ considerably. However, as the rGO@CFRP supports are prepared in identical ways, we believe that the variations in the uniformity of the reduced GO layer cannot explain pronounced differences in the obtained results. Therefore, it can be assumed that the support dictates the deposition process that is consequently determined by the differences of metal plating conditions, allowing the production of free-standing porous Ni@rGO foils (Figure 8a).

Before proceeding further, we note that the Ni layer grows continuously in the 2D mode and that, in theory, one could obtain extremely thin foils that are somewhat brittle. In contrast, we report formation of fairly flexible and porous free-standing foils with a thickness of 40 ± 10 μm (cf. Figure 8b, for 3D SEM surface reconstruction of the free-standing foil). As can be seen from the presented SEM image, the porosity goes all the way through the depth of the foil, which was also confirmed using optical microscopy (Figure 8c). In particular, optical microscopy suggests a porosity of 14%, with a pore density of 790 mm^{-2}.

To explain the differences in the formation of the free-standing foils, we discuss the interactions of metal atoms with the rGO@CFRP support. As the support has partially restored the π electronic system and a large number of defects (cf. Raman spectra), we consider two limiting cases of Cu and Ni atom interactions with pristine graphene and single vacancy in graphene. For the discussion, we use adsorption energy databases in refs 28, 30 and cohesive energies of bulk Cu and Ni of 3.49 and 4.44 eV, respectively.[31,32] In the case of Cu, the adsorption energies on both pristine and monovacant graphene are smaller or similar to the cohesive energy. This leads to the island growth of Cu deposits, as metal−metal interactions are favored. In the initial deposition steps, Cu will preferably bind to other adsorbed Cu atoms, making the nucleation rate of Cu on rGO small and the deposition uneven (see Figure 9, steps I to IV). In the case of Ni, the deposition is expected to be more homogeneous on the CFRP surface because the Ni atoms will preferably bind to defects in rGO, as Ni adsorption energy on defects is larger than Ni cohesive energy.[28] Consequently, the rate of Ni nucleation on rGO is assumed to be increased (compared to Cu) that is

https://doi.org/10.1021/acsomega.1c06145
ACS Omega 2022, 7, 4352−4362

accompanied by higher overpotentials and smaller crystallites that are formed. This is supported by XRD, showing crystallite sizes of about 17 nm in the Ni deposit compared to 250 nm in the case of Cu. In contrast to Ni, the electrodeposition of Cu on reduced GO shows preferentially 3D growth (cf. Figure 2) with a particle size up to several μm. We suspect that the differences in the metal−metal and metal−rGO interactions, resulting in different growth modes of Cu and Ni, could also result in different growth modes in the cases of other metals. While it is difficult to give exact predictions for a complex process such as electrodeposition, we speculate that at least for Ag and Au, one can expect similar growth as for Cu, as the interaction of these metals with rGO is generally weak.[28,30] In contrast, it is likely that metals showing similar (electro)-chemistry to Ni, like Co, will show 2D growth. We also note that other types of defects could contribute to tuning of the growth of the metallic layer. Namely, rGO possesses a certain fraction of oxygen functional groups that can present the centers of enhanced reactivity and nucleation for metal atoms. In our case, the rGO layers were prepared in identical ways for Ni and Cu deposition, but one might expect that the C/O ratio can also be used as an additional parameter for controlling the metal layer growth. However, we believe that such deposition tuning should be done carefully because with decreasing C/O ratio, the conductivity also decreases, indicating that GO is an insulator.[18] Thus, the starting premise, the formation of a conductive layer, would not hold anymore, and we suggest that fully reduced GO should be used for the described synthesis of Ni@rGO foils. Still, we do not exclude local differences in the quality and uniformity of rGO on different locations over CFRP with initially different conductivities as noted in the vicinity of the carbon fiber areas, thus affecting achieved porosity. However, it should be noted that CFRP with directly reduced G on its surface was prepared in a similar manner and that observed differences in Cu and Ni growth are a direct consequence of differences in the interaction with the rGO@CFRP substate and nucleation and growth of electrodeposited layers.

Consecutive steps to describe metal electrodeposition are schematically presented in Figure 9, assuming that in the initial step, the edges of the noncontinuous rGO layer are affected and become more chemically active upon immersion into the electrolyte. (Figure 9I). In the next step, the act of current in the electrolyte causes nucleation of metallic particles on or between the rGO sheets (Figure 9II), leading in the last step to the metal structure built-up on the surface (Figure 9IV). Particles (as visible in Figure 6b in the case of Ni) are mainly located between wrinkled sheets and their edges of rGO. The size of these particles should remain the same regardless of the deposition time, as once the metallic layer is formed, the further supply of the electrolyte is blocked. In the case of Ni, it should be mentioned that HER accompanies the metal deposition from the moment first Ni deposits are formed, providing catalytically active sites for HER (due to the negative overpotentials, Figure 9III). Due to the confirmed synergism between Ni and rGO, the HER rate will even increase progressively, and H_2 bubbles will intensively form.[33] Therefore, it is expected that H_2 bubbles coalesce into the growing Ni layer and represent the barrier for further metal growth (cf. Figure 9III).[33,34] The presence of H_2 bubbles will lead to reduced adhesion of the Ni@rGO layer to the CFRP substrate. This is supported by the fact that the porous Ni@rGO composite foil detaches easily from rGO@CFRP. In addition, pores are present in the deposit on the site where H_2 bubbles were attached (Figure 9IV). The porous metallic Ni layer formed around growing H_2 bubbles shows the smallest crystallite size and the highest internal strains (cf. Figure 5), indicating an increased nucleation rate and reduced growth by the presence of H_2 bubbles, further stimulating the formation of small, highly defective crystallites.

CONCLUSIONS

The modified CFRP composite support made conductive by chemical deposition and reduction of GO directly on its surface provides new insights into the electrodeposition of pure Cu and Ni metals. As a result of different deposition modes and adhesion on the identically treated rGO composite substrate, a free-standing porous Ni@rGO foil and 3D supported Cu@rGO composite structures can be achieved. The difference in deposition is also reflected in the crystallite size of the Cu and Ni deposit and their mechanical properties. The highly defective structure of rGO on CFRP also promoting the metal deposition along with its modification after the deposition is derived from the intensity and shift of peaks in Raman spectra. Based on the results obtained from various methods, a model of the deposition processes on the chemically rGO-modified CFRP surface is given: deposition is governed by the interactions of the metal with defective rGO, which defines the mode of deposit growth and hydrogen evolution taking place at different rates under the operating constant rate deposition conditions. In the case of Ni, deposition results in the formation of free-standing Ni@rGO foils, which could have high potential for practical applications, for example, as current collectors and electrocatalysts. These practical aspects are intensively investigated, and the performance of the Ni@rGO foils will be related to their physical and chemical properties described here.

EXPERIMENTAL SECTION

rGO Preparation. Graphite oxide was prepared by the oxidative treatment of the graphite by a method originally developed by Hummers, further modified and used for chemical synthesis of graphene-based nanosheets.[8,9] Following the exfoliation in water under ultrasonication, produced GO was in the next step transferred directly onto the CFRP surface. Finally, the reduction of GO on CFRP was done by adding hydrazine hydrate and heating in an oven at 80 °C for 24 h.

Metallization Experiments. Electrodeposition of Cu was done using the laboratory (10V/50A) power source (Munk, Germany) at room temperature and a constant current density of 30 mA cm^{-2} using a CuprAcid 210 bath from Atotech (Germany). The calculated thickness of the layer was around 25 μm. In the case of Ni, electrodeposition was also carried out in the galvanostatic mode at 50 mA cm^{-2}, a temperature of 55 °C, and pH = 4.2 from self-formulated Watt's bath for 30 min yielding a thickness of approx. 20 μm of the fully dense deposited layer. After the selected time of deposition in the galvanic Cu or Ni bath, the sample was removed and thoroughly rinsed with deionized water and dried under compressed air.

Spectroscopic Characterization. Raman spectra were obtained using a Horiba Jobin Yvon LabRamHR-VIS system using a green laser at a wavelength of 532 nm with a hole diameter of 500 μm and a lit width of 200 μm. The total signal integration time was 60 s with averaging of 2 scans over the

https://doi.org/10.1021/acsomega.1c06145
ACS Omega 2022, 7, 4352−4362

900−3000 cm^{-1} region. LabSpec software (v.5.19.17, Horiba) was used to acquire spectra, perform background subtraction, and analyze the spectra.[35,36]

Electric Characterization of rGO-Modified CFRP Supports. The impedance experiments were performed on the samples with a total electroactive surface area of 1 cm^2. This analysis could be accomplished while the sample remained in the SEM chamber under the high vacuum measurement conditions. Therefore, the CFRP material was contacted by two W needles, which can be exactly positioned using a micromanipulator (MM3A-EM micromanipulator, Kleindick).[37] The impedance measurements were done using a Voltalab PGZ 301, Radiometer analytical, France. The AC amplitude was 100 mV, and the frequency range was set to 100 kHz to 2 Hz.

Structural Characterization. X-ray powder diffraction (XRD) analysis was carried out using an MPD diffractometer (Philips, NL) with Cu Kα radiation (40 kV/30 mA). The crystallite size and assignment of each peak in the spectrum, labeled by the Miller indices of the planes that diffract the X-rays by Bragg diffraction, were done using Rietveld refinement.

Microscopic Characterization. To analyze the surface, topology, morphology, and composition of composites, rGO interfaces, and metallized rGO@Cu and rGO@Ni layers, electron microscopy was used. A scanning electron microscope (SEM), ZEISS SIGMA HD VP device, with imaging resolution as small as 1 nm, was used. The samples were measured without additional coating. For the detailed structural characterization of the Ni deposit, the samples were thinned to electron transparency by argon ion milling and investigated by transmission electron microscopy (TEM). The TEM study was carried out with a Philips CM200 equipped with a Gatan Orius CCD camera and energy-dispersive X-ray spectrometry (EDX) for chemical analysis. Bright-field, dark-field, and diffraction images were taken to characterize different areas. In addition, background-subtracted intensity profiles of the diffraction pattern were calculated by integration along the rings and analyzed quantitatively using the software PASAD-tools.[38] To investigate the Ni@rGO foil porosity and thickness, SEM 3D reconstruction was done using a Phenom ProX scanning electron microscope, while optical microscopy was performed using an optical microscope Olympus BX51. To evaluate the porosity, optical microscopy images were processed using Olympus Stream software.

Adhesion of Metallized rGO@CFRP Supports. Qualitative adhesion tests were carried out by cross-cut testing according to a standardized procedure "paints and varnishes—cross-cut test" (ISO 2409). The distance between the blades was set to1 mm. Then, the layer on the sample was cut perpendicular horizontally and vertically at 90° to form a square lattice pattern of fine cuts.

Evaluation of Mechanical Properties. Nanoindentation was performed on the cross section of the electrodeposited Cu and Ni and on top of the as-received and rGO-modified CFRP supports. The nanoindentation was carried out using an ASMEC Unat with a Berkovich tip. To test for surface effects, depth dependence profiles of hardness and Young's modulus were acquired using the quasi-continuous stiffness measurement (QCSM) method. Indents were carefully positioned under an optical microscope on the substrate surface. By calculating the contact stiffness from the force and displacement amplitudes of oscillations at different loads, the indentation hardness as a function of depth can be evaluated on a single location of the sample.[39] A maximal force of up to 50 mN with a quadratic loading function was used for both Cu and Ni deposited on the rGO@CFRP-modified surface.

■ ASSOCIATED CONTENT

Supporting Information

The Supporting Information is available free of charge at https://pubs.acs.org/doi/10.1021/acsomega.1c06145.

Electrical characterization of rGO-modified CFRP substrates (Figure S1); microscopic characterization of the top surface and the cross section of the CFRP substrate (Figure S2); evaluation of mechanical properties: nanoindentation measurements of bare, rGO-modified and metallized Cu and Ni CFRP supports (Figure S3); and XRD patterns of unmodified and electrodeposited Cu and Ni on rGO-modified CFRP composite supports (Figure S4) (PDF)

■ AUTHOR INFORMATION

Corresponding Author

Lidija D. Rafailović − *CEST, Center of Electrochemical Surface Technology, Wiener Neustadt 2700, Austria;* Present Address: University of Leoben, Department of Materials Science, Chair of Materials Physics, Jahnstrasse 12, 8700 Leoben, Austria; orcid.org/0000-0002-9643-9338; Email: lidija.rafailovic@unileoben.ac.at

Authors

Aleksandar Z. Jovanović − *Faculty of Physical Chemistry, University of Belgrade, Belgrade 11158, Serbia;* orcid.org/0000-0003-1505-838X

Sanjin J. Gutić − *Faculty of Science, Department of Chemistry, University of Sarajevo, Sarajevo 71000, Bosnia and Herzegovina;* orcid.org/0000-0002-5780-8022

Jürgen Wehr − *Airbus Defence and Space GmbH, Taufkirchen 82024, Germany*

Christian Rentenberger − *Faculty of Physics, Physics of Nanostructured Materials, University of Vienna, Vienna 1090, Austria*

Tomislav Lj. Trišović − *Institute of Technical Sciences of the Serbian Academy of Sciences and Arts, Belgrade 11000, Serbia*

Igor A. Pašti − *Faculty of Physical Chemistry, University of Belgrade, Belgrade 11158, Serbia;* orcid.org/0000-0002-1000-9784

Complete contact information is available at: https://pubs.acs.org/10.1021/acsomega.1c06145

Author Contributions

The manuscript was written through contributions of all authors. All authors have given approval to the final version of the manuscript.

Notes

The authors declare no competing financial interest.

■ ACKNOWLEDGMENTS

This work was supported by the COMET program by the Austrian Research Promotion Agency (FFG) and the governments of Lower and Upper Austria. L.D.R. and S.J.G. acknowledge in addition the support given by the Federal Ministry Republic of Austria within the framework of Scientific and Technological Cooperation (OeAD Project No. BIH 07/

2019). A.Z.J. and I.A.P. acknowledge the support provided by the Serbian Ministry of Education, Science, and Technological Development (Contract No. 451-03-9/2021-14/200146) and the Science Fund of the Republic of Serbia (project RatioCAT, No. 606224). This work was also sponsored in part by the NATO Science for Peace and Security Program under grant G5729. The authors would like to thank C. Kleber and C. Kotlowski for help with GO substrate modification, J. Wosik for SEM, A. Gavrilovic-Wohlmuther for XRD, and G. Polt for nanoindentation measurements.

REFERENCES

(1) Novoselov, K. S.; Geim, A. K.; Morozov, S. V.; Jiang, D.; Zhang, Y.; Dubonos, S. V.; Grigorieva, I. V.; Firsov, A. A. Electric Field Effect in Atomically Thin Carbon Films. *Science* **2004**, *306*, 666−669.
(2) Eda, G.; Lin, Y.-Y.; Miller, S.; Chen, C.-W.; Su, W.-F.; Chhowalla, M. Transparent and Conducting Electrodes for Organic Electronics from Reduced Graphene Oxide. *Appl. Phys. Lett.* **2008**, *92*, No. 233305.
(3) Fang, M.; Wang, K.; Lu, H.; Yang, Y.; Nutt, S. Covalent Polymer Functionalization of Graphene Nanosheets and Mechanical Properties of Composites. *J. Mater. Chem.* **2009**, *19*, 7098−7105.
(4) Chen, D.; Tang, L.; Li, J. Graphene-Based Materials in Electrochemistry. *Chem. Soc. Rev.* **2010**, *39*, 3157−3180.
(5) Zhu, Y.; Murali, S.; Cai, W.; Li, X.; Suk, J. W.; Potts, J. R.; Ruoff, R. S. Graphene and Graphene Oxide: Synthesis, Properties, and Applications. *Adv. Mater.* **2010**, *22*, 3906−3924.
(6) Cai, M.; Thorpe, D.; Adamson, D. H.; Schniepp, H. C. Methods of Graphite Exfoliation. *J. Mater. Chem.* **2012**, *22*, 24992−25002.
(7) Pei, S.; Cheng, H. M. The Reduction of Graphene Oxide. *Carbon* **2012**, *50*, 3210−3228.
(8) Hummers, W. S.; Offeman, R. E. Preparation of Graphitic Oxide. *J. Am. Chem. Soc.* **1958**, *80*, No. 1339.
(9) Stankovich, S.; Dikin, D. A.; Piner, R. D.; Kohlhaas, K. A.; Kleinhammes, A.; Jia, Y.; Wu, Y.; Nguyen, S. T.; Ruoff, R. S. Synthesis of Graphene-Based Nanosheets via Chemical Reduction of Exfoliated Graphite Oxide. *Carbon* **2007**, *45*, 1558−1565.
(10) Chanda, D.; Hnát, J.; Dobrota, A. S.; Pašti, I. A.; Paidar, M.; Bouzek, K. The Effect of Surface Modification by Reduced Graphene Oxide on the Electrocatalytic Activity of Nickel towards the Hydrogen Evolution Reaction. *Phys. Chem. Chem. Phys.* **2015**, *17*, 26864−26874.
(11) Gutić, S. J.; Jovanović, A. Z.; Dobrota, A. S.; Metarapi, D.; Rafailović, L. D.; Pašti, I. A.; Mentus, S. V. Simple Routes for the Improvement of Hydrogen Evolution Activity of Ni-Mo Catalysts: From Sol-Gel Derived Powder Catalysts to Graphene Supported Co-Electrodeposits. *Int. J. Hydrogen Energy* **2018**, *43*, 16846−16858.
(12) Lammel, P.; Rafailovic, L. D.; Kolb, M.; Pohl, K.; Whitehead, A. H.; Grundmeier, G.; Gollas, B. Analysis of Rain Erosion Resistance of Electroplated Nickel-Tungsten Alloy Coatings. *Surf. Coat. Technol.* **2012**, *206*, 2545−2551.
(13) Prysiazhnyi, V.; Stupavská, M.; Ráheľ, J.; Kleber, C.; Černák, M.; Rafailović, L. D. A Comparison of Chemical and Atmospheric Plasma Assisted Copper Plating on Carbon Fiber Reinforced Epoxy Polymer Surfaces. *Surf. Coat. Technol.* **2014**, *258*, 1082−1089.
(14) Sun, Y. *Mechanical Properties of Carbon Nanotube/Metal Composites*, University of Central Florida, 2010.
(15) Ferrari, A. C.; Meyer, J. C.; Scardaci, V.; Casiraghi, C.; Lazzeri, M.; Mauri, F.; Piscanec, S.; Jiang, D.; Novoselov, K. S.; Roth, S.; Geim, A. K. Raman Spectrum of Graphene and Graphene Layers. *Phys. Rev. Lett.* **2006**, *97*, No. 187401.
(16) Claramunt, S.; Varea, A.; López-Díaz, D.; Velázquez, M. M.; Cornet, A.; Cirera, A. The Importance of Interbands on the Interpretation of the Raman Spectrum of Graphene Oxide. *J. Phys. Chem. C* **2015**, *119*, 10123−10129.
(17) Eckmann, A.; Felten, A.; Mishchenko, A.; Britnell, L.; Krupke, R.; Novoselov, K. S.; Casiraghi, C. Probing the Nature of Defects in Graphene by Raman Spectroscopy. *Nano Lett.* **2012**, *12*, 3925−3930.
(18) Eckmann, A.; Felten, A.; Verzhbitskiy, I.; Davey, R.; Casiraghi, C. Raman Study on Defective Graphene: Effect of the Excitation Energy, Type, and Amount of Defects. *Phys. Rev. B* **2013**, *88*, No. 035426.
(19) Levy, R. L.; Schwab, S. D. Monitoring the Composite Curing Process with a Fluorescence-Based Fiber-Optic Sensor. *Polym. Compos.* **1991**, *12*, 96−101.
(20) Gao, X.; Jang, J.; Nagase, S. Hydrazine and Thermal Reduction of Graphene Oxide: Reaction Mechanisms, Product Structures, and Reaction Design. *J. Phys. Chem. C* **2010**, *114*, 832−842.
(21) Toh, S. Y.; Loh, K. S.; Kamarudin, S. K.; Daud, W. R. W. Graphene Production via Electrochemical Reduction of Graphene Oxide: Synthesis and Characterisation. *Chem. Eng. J.* **2014**, *251*, 422−434.
(22) Radisic, A.; Vereecken, P. M.; Searson, P. C.; Ross, F. M. The Morphology and Nucleation Kinetics of Copper Islands during Electrodeposition. *Surf. Sci.* **2006**, *600*, 1817−1826.
(23) Lotfi, N.; Shahrabi, T.; Yaghoubinezhad, Y.; Darband, G. B. Direct Electrodeposition of Platinum Nanoparticles@graphene Oxide@nickel-Copper@nickel Foam Electrode as a Durable and Cost-Effective Catalyst with Remarkable Performance for Electrochemical Hydrogen Evolution Reaction. *Appl. Surf. Sci.* **2020**, *505*, No. 144571.
(24) Williamson, G.; Hall, W. X-Ray Line Broadening from Filed Aluminium and Wolfram. *Acta Metall.* **1953**, *1*, 22−31.
(25) Wang, W. X.; Liang, S. H.; Yu, T.; Li, D. H.; Li, Y. B.; Han, X. F. The Study of Interaction between Graphene and Metals by Raman Spectroscopy. *J. Appl. Phys.* **2011**, *109*, No. 07C501.
(26) Zheng, X.; Chen, W.; Wang, G.; Yu, Y.; Qin, S.; Fang, J.; Wang, F.; Zhang, X.-A. The Raman Redshift of Graphene Impacted by Gold Nanoparticles. *AIP Adv.* **2015**, *5*, No. 057133.
(27) Iqbal, M. W.; Singh, A. K.; Iqbal, M. Z.; Eom, J. Raman Fingerprint of Doping Due to Metal Adsorbates on Graphene. *J. Phys. Condens. Matter* **2012**, *24*, No. 335301.
(28) Pašti, I. A.; Jovanović, A.; Dobrota, A. S.; Mentus, S. V.; Johansson, B.; Skorodumova, N. V. Atomic Adsorption on Pristine Graphene along the Periodic Table of Elements − From PBE to Non-Local Functionals. *Appl. Surf. Sci.* **2018**, *436*, 433−440.
(29) Jovanović, Z.; Pašti, I.; Kalijadis, A.; Jovanović, S.; Laušević, Z. Platinum-Mediated Healing of Defective Graphene Produced by Irradiating Glassy Carbon with a Hydrogen Ion-Beam. *Mater. Chem. Phys.* **2013**, *141*, 27−34.
(30) Pašti, I. A.; Jovanović, A.; Dobrota, A. S.; Mentus, S. V.; Johansson, B.; Skorodumova, N. V. Atomic Adsorption on Graphene with a Single Vacancy: Systematic DFT Study through the Periodic Table of Elements. *Phys. Chem. Chem. Phys.* **2018**, *20*, 858−865.
(31) Kittel, C. *Solid State Physics*, 8th ed., John Wiley and Sons, New York, 2004.
(32) Kaxiras, E. *Atomic and Electronic Structure of Solids*, Cambridge University Press, 2003.
(33) Gutić, S. J.; Dobrota, A. S.; Leetmaa, M.; Skorodumova, N. V.; Mentus, S. V.; Pašti, I. A. Improved Catalysts for Hydrogen Evolution Reaction in Alkaline Solutions through the Electrochemical Formation of Nickel-Reduced Graphene Oxide Interface. *Phys. Chem. Chem. Phys.* **2017**, *19*, 13281−13293.
(34) Rafailović, L. D.; Rentenberger, C.; Kleber, C.; Whitehead, A. H.; Gollas, B.; Karnthaler, H. P.; et al. Preparation of CoNi High Surface Area Porous Foams by Substrate Controlled Electrodeposition. *Phys. Chem. Chem. Phys.* **2012**, *14*, 972−980.
(35) Rafailović, L. D.; Gammer, C.; Srajer, J.; Trišović, T.; Rahel, J.; Karnthaler, H. P. Surface Enhanced Raman Scattering of Dendritic Ag Nanostructures Grown with Anodic Aluminium Oxide. *RSC Adv.* **2016**, *6*, 33348−33352.
(36) Rafailović, L. D.; Gammer, C.; Rentenberger, C.; Trišović, T.; Kleber, C.; Karnthaler, H. P. Functionalizing Aluminum Oxide by Ag Dendrite Deposition at the Anode during Simultaneous Electrochemical Oxidation of Al. *Adv. Mater.* **2015**, *27*, 6438−6443.
(37) Chen, Q.; Wang, S.; Peng, L.-M. Establishing Ohmic Contacts for in Situ Current−Voltage Characteristic Measurements on a

https://doi.org/10.1021/acsomega.1c06145
ACS Omega 2022, 7, 4352−4362

Carbon Nanotube inside the Scanning Electron Microscope. *Nanotechnology* **2006**, *17*, 1087−1098.
(38) Gammer, C.; Mangler, C.; Rentenberger, C.; Karnthaler, H. P. Quantitative Local Profile Analysis of Nanomaterials by Electron Diffraction. *Scr. Mater.* **2010**, *63*, 312−315.
(39) Hay, J.; Agee, P.; Herbert, E. Continuous Stiffness Measurement during Instrumented Indentation Testing. *Exp. Tech.* **2010**, *34*, 86−94.

https://doi.org/10.1021/acsomega.1c06145
ACS Omega 2022, 7, 4352−4362